X-RAY CAVITIES IN A SAMPLE OF 83 SPT-SELECTED CLUSTERS OF GALAXIES: TRACING THE EVOLUTION OF AGN FEEDBACK IN CLUSTERS OF GALAXIES OUT TO z = 1.2

Citation: Hlavacek-Larrondo, J., M. McDonald, B. A. Benson, W. R. Forman, S. W. Allen, L. E. Bleem, M. L. N. Ashby, et al. "X-RAY CAVITIES IN A SAMPLE OF 83 SPT-SELECTED CLUSTERS OF GALAXIES: TRACING THE EVOLUTION OF AGN FEEDBACK IN CLUSTERS OF GALAXIES OUT TO z = 1.2." The Astrophysical Journal 805, no. 1 (May 18, 2015): 35. © 2015 The American Astronomical Society

As Published: http://dx.doi.org/10.1088/0004-637x/805/1/35

Publisher: IOP Publishing

Persistent URL: http://hdl.handle.net/1721.1/98367

Version: Final published version: final published article, as it appeared in a journal, conference proceedings, or other formally published context

The Astrophysical Journal, 805:35 (13pp), 2015 May 20 doi:10.1088/0004-637X/805/1/35

X-RAY CAVITIES IN A SAMPLE OF 83 SPT-SELECTED CLUSTERS OF GALAXIES: TRACING THE EVOLUTION OF AGN FEEDBACK IN CLUSTERS OF GALAXIES OUT TO $z = 1.2$

J. Hlavacek-Larrondo[1,2,3], M. McDonald[4], B. A. Benson[5,6,7], W. R. Forman[8], S. W. Allen[2,3,9], L. E. Bleem[5,10,11], M. L. N. Ashby[8], S. Bocquet[12,13], M. Brodwin[14], J. P. Dietrich[12,13], C. Jones[8], J. Liu[12,13], C. L. Reichardt[15,16], B. R. Saliwanchik[17], A. Saro[12], T. Schrabback[18], J. Song[19,20], B. Stalder[8,21], A. Vikhlinin[8], and A. Zenteno[12,22]
[1] Département de Physique, Université de Montréal, C.P. 6128, Succ. Centre-Ville, Montreal, Quebec H3C 3J7, Canada; juliehl@astro.umontreal.ca
[2] Kavli Institute for Particle Astrophysics and Cosmology, Stanford University, 452 Lomita Mall, Stanford, CA 94305, USA
[3] Department of Physics, Stanford University, 382 Via Pueblo Mall, Stanford, CA 94305, USA
[4] Kavli Institute for Astrophysics and Space Research, Massachusetts Institute of Technology, 77 Massachusetts Avenue, Cambridge, MA 02139, USA
[5] Kavli Institute for Cosmological Physics, University of Chicago, 5640 South Ellis Avenue, Chicago, IL 60637, USA
[6] Fermi National Accelerator Laboratory, Batavia, IL 60510-0500, USA
[7] Department of Astronomy and Astrophysics, University of Chicago, 5640 South Ellis Avenue, Chicago, IL 60637, USA
[8] Harvard-Smithsonian Center for Astrophysics, 60 Garden Street, Cambridge, MA 02138, USA
[9] SLAC National Accelerator Laboratory, 2575 Sand Hill Road, Menlo Park, CA 94025, USA
[10] Argonne National Laboratory, High-Energy Physics Division, 9700 S. Cass Avenue, Argonne, IL 60439, USA
[11] Department of Physics, University of Chicago, 56 Ellis Avenue, Chicago, IL 60637, USA
[12] Department of Physics, Ludwig-Maximilians-Universität, Scheinerstr. 1, D-81679 München, Germany
[13] Excellence Cluster universe, Boltzmannstr. 2, D-85748 Garching, Germany
[14] Department of Physics and Astronomy, University of Missouri, 5110 Rockhill Road, Kansas City, MO 64110, USA
[15] Department of Physics, University of California, Berkeley, CA 94720, USA
[16] School of Physics, University of Melbourne, Parkville, VIC 3010, Australia
[17] Physics Department, Center for Education and Research in Cosmology and Astrophysics, Case Western Reserve University, Cleveland, OH 44106, USA
[18] Argelander-Institut für Astronomie, Auf dem Hügel 71, D-53121 Bonn, Germany
[19] Department of Physics, University of Michigan, 450 Church Street, Ann Arbor, MI, 48109, USA
[20] Korea Astronomy & Space Science Institute, Daejeon, Korea
[21] Institute for Astronomy, University of Hawaii at Manoa, Honolulu, HI 96822, USA
[22] Cerro Tololo Inter-American Observatory, Casilla 603, La Serena, Chile
Received 2014 September 18; accepted 2015 March 4; published 2015 May 18

ABSTRACT

X-ray cavities are key tracers of mechanical (or radio mode) heating arising from the active galactic nuclei (AGNs) in brightest cluster galaxies (BCGs). We report on a survey for X-ray cavities in 83 massive, high-redshift ($0.4 < z < 1.2$) clusters of galaxies selected by their Sunyaev-Zel'dovich signature in the South Pole Telescope data. Based on *Chandra* X-ray images, we find a total of six clusters having symmetric pairs of surface brightness depressions consistent with the picture of radio jets inflating X-ray cavities in the intracluster medium (ICM). The majority of these detections are of relatively low significance and require deeper follow-up data in order to be confirmed. Further, this search will miss small (<10 kpc) X-ray cavities that are unresolved by *Chandra* at high ($z \gtrsim 0.5$) redshift. Despite these limitations, our results suggest that the power generated by AGN feedback in BCGs has remained unchanged for over half of the age of the universe (>7 Gyr at $z \sim 0.8$). On average, the detected X-ray cavities have powers of $(0.8-5) \times 10^{45}$ erg s^{-1}, enthalpies of $(3-6) \times 10^{59}$ erg, and radii of ~17 kpc. Integrating over 7 Gyr, we find that the supermassive black holes in BCGs may have accreted 10^8 to several 10^9 $M_\odot$ of material to power these outflows. This level of accretion indicates that significant supermassive black hole growth may occur not only at early times, in the quasar era, but at late times as well. We also find that X-ray cavities at high redshift may inject an excess heat of 0.1–1.0 keV per particle into the hot ICM above and beyond the energy needed to offset cooling. Although this result needs to be confirmed, we note that the magnitude of excess heating is similar to the energy needed to preheat clusters, break self-similarity, and explain the excess entropy in hot atmospheres.

Key words: black hole physics – galaxies: clusters: general – galaxies: jets – X-rays: galaxies: clusters

1. INTRODUCTION

The observed correlations between supermassive black hole mass and galaxy bulge properties such as stellar velocity dispersion (e.g., Ferrarese & Merritt 2000; Gebhardt et al. 2000), spheroid mass (e.g., Kormendy & Richstone 1995), and spheroid luminosity (e.g., Magorrian et al. 1998) strongly suggest that supermassive black holes and their host galaxies grew in concert with one another (see Alexander & Hickox 2012). The majority of the growth of these black holes occurs at high redshifts ($z \gtrsim 1$) when they are accreting at rates near the Eddington limit, leading to powerful radiative or "quasar-mode" feedback (e.g., Fabian 2012). It is thought that this mode of feedback from active galactic nuclei (AGNs) in the early universe has led to the aforementioned correlations (e.g., Di Matteo et al. 2005; Springel et al. 2005; Croton et al. 2006).

In direct contrast, local supermassive black holes are generally accreting at rates well below 1% of the Eddington limit. A large fraction of these black holes appear to be driving powerful jetted outflows that often extend beyond the galactic hosts (e.g., Körding et al. 2006). The low accretion rates of these black holes imply that they are most likely powered by advection-dominated accretion flows (Narayan & Yi 1994, and references therein). In contrast to radiation-dominated, "quasar-

mode" feedback, these systems are providing mechanically dominated "radio-mode" feedback (e.g., McNamara & Nulsen 2012). It remains unclear how and why supermassive black holes switch from one mode to the other over cosmic time.

Hlavacek-Larrondo et al. (2012, 2013, hereafter HL12 and HL13, respectively) recently attempted to answer this question by targeting high-redshift ($z > 0.3$) brightest cluster galaxies (BCGs). The AGNs in these massive galaxies provide some of the most compelling cases for radio-mode feedback. Jetted outflows are often seen to emerge from the AGNs in BCGs, and as they propagate through the hot X-ray-emitting intracluster medium (ICM), they push aside the ICM-creating regions of depleted X-ray emission known as X-ray cavities (or bubbles). These X-ray cavities provide a unique opportunity to directly measure the work done by "radio-mode" AGN feedback on the surrounding medium (e.g., Bîrzan et al. 2004, 2008; Dunn et al. 2005, 2010; Dunn & Fabian 2006, 2008; Rafferty et al. 2006; Nulsen et al. 2007; Cavagnolo et al. 2010; Dong et al. 2010; O'Sullivan et al. 2011). In particular, HL12 and HL13 showed that the AGNs in BCGs were becoming increasingly more X-ray luminous with redshift while the mechanical properties of their outflows—as characterized by the properties of their X-ray cavities—remain unchanged. In other words, HL12 and HL13 were directly witnessing the transition between quasar-mode feedback and radio-mode feedback (see also Ma et al. 2011, 2013; Ueda et al. 2013).

HL12 and HL13 based their study on the MAssive Cluster Survey (MACS), a survey consisting of highly X-ray-luminous clusters at $0.3 < z < 0.7$ (Ebeling et al. 2001, 2007, 2010), but the MACS sample contains only four clusters with *Chandra* X-ray observations beyond $z = 0.55$; to constrain the evolution of AGN feedback in BCGs beyond $z = 0.55$, a larger sample of high-redshift clusters is required. Such measurements are possible since *Chandra*, with a point-spread function of $\sim 1''$, has the potential to resolve and identify X-ray cavities out to $z \sim 1.0$.[23] Indeed, X-ray cavities in massive clusters have typical radii of 15–20 kpc (see Figure 4 in McNamara & Nulsen 2007 and Figure 8 in HL12), corresponding to $2''$–$2''.5$ at $z = 1.0$.

Recently, the number of known high-redshift galaxy clusters has increased dramatically, largely due to the success of large mm-wave surveys utilizing the Sunyaev-Zel'dovich (SZ) effect to select massive clusters at all redshifts. These SZ surveys include the South Pole Telescope (SPT) (Staniszewski et al. 2009; Vanderlinde et al. 2010; Reichardt et al. 2013; Bleem et al. 2015), the *Planck* satellite (Planck Collaboration 2011, Planck-29 2013), and the Atacama Cosmology Telescope (Marriage et al. 2011; Sifon et al. 2013; Hasselfield et al. 2013). Since the surface brightness of the SZ effect is redshift independent, SZ surveys have the potential to select nearly mass-limited cluster samples out to the earliest epochs of cluster formation. This is in contrast to previous surveys, such as those based on X-ray selection methods (e.g., Gioia & Luppino 1994; Burenin et al. 2007), which have strong redshift-dependent selection functions from cosmological dimming (Figure 1). The 2500 deg^2 SPT–SZ cluster survey (Bleem et al. 2015) in particular contains 83 massive clusters at $0.3 < z < 1.2$ that have now been observed with *Chandra* (e.g., McDonald et al. 2013a, hereafter M13). By examining the *Chandra* X-ray images of these 83 SPT–SZ clusters, we aim to extend the sample of known clusters of galaxies with X-ray cavities out to $z \sim 1$. This will allow us to determine if AGN feedback is indeed operating differently at high redshift as suggested by HL12 and HL13.

In this paper we focus on the X-ray cavity properties—the AGN radiative properties will be explored in a future paper. In Section 2, we present the *Chandra* X-ray data, then in Section 3 we describe the method for identifying X-ray cavities. In Section 4, we explain how we calculate cooling luminosities. Finally, in Section 5 we present the results, and we discuss them in Section 6. We state the conclusions in Section 7. Throughout this paper, we adopt $H_0 = 70$ km s^{-1} Mpc^{-1} with $\Omega_m = 0.3$ and $\Omega_\Lambda = 0.7$. All errors are 1σ unless otherwise noted.

2. X-RAY OBSERVATIONS AND DATA REDUCTION

The majority of the SPT–SZ clusters with *Chandra* X-ray data were observed through a *Chandra* X-ray Visionary Project (XVP, PI Benson) targeting the most significant ($\xi > 6.5$) SZ detections in the first 2000 deg^2 of the 2500 deg^2 SPT–SZ survey at $z > 0.4$ (Benson et al. 2013). The XVP exposure times were chosen to obtain ~2000 X-ray counts per cluster, predicted using an SPT significance to X-ray luminosity relation from a subset of clusters with earlier *Chandra* observations. While a total of 80 clusters were observed through this XVP, we only consider the 74 that were observed with *Chandra* and not the 6 that were observed with *XMM-Newton*, since *Chandra* is the only telescope that can resolve X-ray cavities at high redshifts. In addition to these 74 clusters, we include nine SPT-selected clusters at $z > 0.3$ that were previously observed through other *Chandra* programs.

The final sample therefore consists of 83 massive clusters, spanning a redshift range of $0.3 \leqslant z \leqslant 1.2$. These clusters all have highly significant SPT detections ($\xi > 6.5$), and we expect the SZ selection to be nearly mass independent with no significant detection bias toward clusters with highly peaked surface brightness distributions (Motl et al. 2005).

The majority of the X-ray data reduction and analysis is described in M13, to which we refer the reader for a more detailed description. Briefly, surface brightness profiles are measured in a series of 20 annuli out to $1.5 \times R_{500}$. These are then expressed as projected emission measure integrals of the gas density, and the latter are modeled using modified beta models (Vikhlinin et al. 2006). With only ~2000 X-ray counts per cluster, one cannot apply the standard deprojection techniques (e.g., Vikhlinin et al. 2006; Sun et al. 2009). Instead, M13 models the underlying dark matter distributions as generalized Navarro–Frenk–White profiles (Zhao 1996; Wyithe et al. 2001). Under the assumption of hydrostatic equilibrium, the authors then produce best-fit deprojected gas density and temperature profiles, along with a model for the underlying gravitational potential for each cluster. While we use these best-fit deprojected profiles throughout the paper, we note that the uncertainties derived in M13 do not reflect the underlying assumptions: typical uncertainties are significantly larger, on the order of 25% in pressure and 50% in the depth of the gravitational potential at the radii of cavities (see Appendix A of M13). Since the local pressure and gravitational potential are two quantities needed to compute X-ray cavity energetics,

[23] We note that *Chandra* actually holds the potential to resolve X-ray cavities of ~20 kpc size out to any redshift, due to the flattening of the angular diameter distance at high redshift in ΛCDM. However, beyond $z \sim 1$, observations become prohibitively expensive due to X-ray surface brightness dimming.

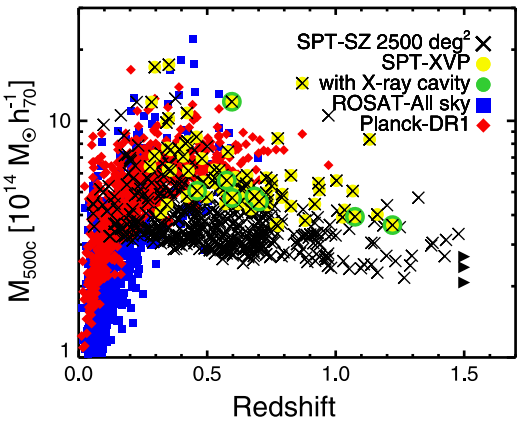

Figure 1. Estimated cluster masses versus redshift for different cluster samples. The mass is defined as M_{500c}, the mass enclosed within a radius at which the average density is 500 times the critical density at the cluster redshift. We highlight in yellow the 83 SPT–SZ clusters with *Chandra* X-ray observations that were analyzed in this study. In green, we further highlight the eight SPT–SZ clusters with candidate X-ray cavities. The right-pointing arrows symbolize the three high-redshift clusters at $z \gtrsim 1.5$ where the *Spitzer* redshift model is poorly constrained.

the reported cavity energetics in the SPT–SZ sample are, at best, within a factor of a few of their true value. We therefore proceed with the search of cavities in the sample while using the values derived in M13, but bear in mind throughout the paper that the uncertainties are significantly larger than reported in M13.

3. IDENTIFYING SYSTEMS WITH X-RAY CAVITIES

3.1. Method

To identify systems with X-ray cavities, we visually search the central 100 kpc of each cluster for circular or ellipsoidal surface brightness depressions in the *Chandra* X-ray images. Past studies on local clusters have found that the majority of X-ray cavities are located within this region (e.g., McNamara & Nulsen 2007, HL12).

As a first indicator, we create unsharp-masked images for each cluster to enhance deviations in the original *Chandra* X-ray image. This method consists of subtracting a strongly smoothed image from a lightly smoothed image and has been used extensively in the literature for X-ray cavity studies (e.g., Blanton et al. 2009; Sanders et al. 2009; Machacek et al. 2011). For the strongly smoothed image, we use Gaussian smoothing scales on the order of 40–80 kpc to match the underlying large-scale cluster emission, and for the lightly smoothed image, we use Gaussian smoothing scales on the order of 5–10 kpc to match the typical length scale of a cavity. Next, we build a best-fitting King model, centered on the X-ray peak, for the surface brightness distribution of all clusters showing hints of depressions. We use the lightly smoothed *Chandra* X-ray image to build the King model and subtracted the resulting King model image from the original *Chandra* X-ray image. We refer to these as the "King-subtracted" images. The King model is defined as

$$I(r) = I_0 \left(1 + \left(\frac{r}{r_0}\right)^2\right)^{-\beta} + C_0, \quad (1)$$

where I_0 is the normalization, r_0 is the core radius, and C_0 is a constant. We allow all three of these parameters to vary while building the King model.

We try several binning and smoothing factors for all clusters and also test the robustness of the King-subtracted method by shifting the position of the central peak by $\pm 2-3$ pixels. We examine three energy bands: 0.5−7 keV, 0.3−2 keV, and 0.6−3 keV. We only consider cavities to be real if they are visually identifiable in all X-ray images, including the original X-ray images (excessive binning and smoothing eventually removes any indication of a depression).

Out of the 83 SPT–SZ clusters with *Chandra* X-ray observations, we find that 10 clusters have surface brightness depressions in their *Chandra* X-ray images. However, to minimize false identification, three co-authors (Hlavacek-Larrondo, McDonald, and Allen) independently classified each cluster based on the visual significance of its X-ray cavities, clusters were classified as having either convincing X-ray cavities, somewhat convincing X-ray cavities, or unconvincing X-ray cavities. We then tabulated the classifications and only kept those that were classified as having convincing or somewhat convincing X-ray cavities by at least two co-authors. This resulted in the rejection of 2 of the original 10 clusters: SPT-CLJ0334–4659 ($z = 0.45$) and SPT-CLJ2043–5035 ($z = 0.7234$).

The final list of clusters with X-ray cavities is shown in Table 1. We note that six of these clusters were unanimously classified as having convincing or somewhat convincing X-ray cavities by all three co-authors. From now on, we refer to these as the clusters with "convincing" X-ray cavities. These are shown in the top portion of Table 1. The remaining two clusters, SPT-CLJ0156–5541 ($z = 1.2$) and SPT-CLJ2342–5411 ($z = 1.075$), were classified as having unconvincing X-ray cavities by one co-author. To emphasize the uncertainty related to these two particular systems, we highlight them differently in all tables (see bottom portion) and figures (square symbols instead of triangles).

The raw, unsharp-masked, and King-subtracted images of the final list of clusters with X-ray cavities are shown in Figure 2. The smoothing and binning factors are indicated in the lower-left corner of each image. "BX" refers to the image binning factor: "B1" means that the image was not binned, whereas "B2" means that each pixel corresponds to 4 pixels in the original image. The smoothing factor is denoted as "SX," where "X" corresponds to the sigma of a Gaussian in units of pixels once the image was binned. For each unsharp-masked image, we show the two smoothing scales used to create the image, and for each King-subtracted image we show the smoothing scale adopted for the original image before creating and subtracting a King model. Those with brackets were additionally smoothed for illustrative purposes. The optical or near-infrared images obtained as part of the SPT 2500 deg^2 follow-up campaign for photometric redshifts are also shown (High et al. 2010; Song et al. 2012; Bleem et al. 2015). These were taken with the *Spitzer Space Telescope*, the Swope 1 m telescope, the CTIO Blanco 4 m telescope, or the Baade Magellan 6.5 m telescope (see Bleem et al. 2015, for details).

The depth of each cavity was estimated in the X-ray data using an azimuthal averaged surface brightness (see Figure 3). We measure azimuthal surface brightness profiles from the X-ray data (left panels of Figure 2), using an annulus that encompassed the cavities, centered on the X-ray peak (middle-

Table 1
SPT–SZ Clusters with Candidate X-ray Cavities

(1) Name	(2) z	(3) $L_{\rm cool\ 7.7Gyrs}$ (10^{44} erg s^{-1})	(4) $L_{\rm cool\ r=50\ kpc}$ (10^{44} erg s^{-1})	(5) $L_{\rm cool\ z=2}$ (10^{44} erg s^{-1})	(6) N	(7) $R_{\rm l}$ (kpc)	(8) $R_{\rm w}$ (kpc)	(9) R (kpc)	(10) PA (^{o})	(11) PV (10^{59} erg)	(12) $P_{\rm cav}$ (10^{44} erg s^{-1})	(13) Radio …
SPT-CLJ0000–5748	0.7019	7.9	5.2	5.0	#1^{P}	18.6	10.7	37	140	1.9 ± 0.8	9.9 ± 5.0	✓
					#2^{P}	15.7	15.7	32	322	3.5 ± 1.6	19.2 ± 9.7	…
SPT-CLJ0033–6326	0.59712	0.7	0.7	0.3	#1^{P}	33.3	20.0	62	100	3.3 ± 1.5	7.7 ± 3.9	✓[a]
					#2^{P}	30.7	23.3	73	280	3.2 ± 1.4	5.6 ± 2.8	
SPT-CLJ0509–5342	0.4607	1.3	1.5	0.9	#1^{C}	16.9	16.9	32	42	1.9 ± 0.8	6.8 ± 3.4	×[b]
					#2^{C}	24.9	13.4	35	223	1.8 ± 0.8	7.1 ± 3.6	…
SPT-CLJ0616–5227	0.6838	1.9	1.6	0.2	#1^{C}	24.0	17.0	62	82	1.7 ± 0.8	2.4 ± 1.2	✓
					#2^{P}	24.0	17.0	37	234	2.2 ± 1.0	5.2 ± 2.6	…
SPT-CLJ2331–5051	0.576	5.5	3.6	3.8	#1^{P}	13.7	10.5	27	59	1.1 ± 0.5	6.4 ± 3.2	✓
					#2^{P}	12.4	9.2	20	222	1.6 ± 0.7	21.3 ± 10.7	…
SPT-CLJ2344–4243[c]	0.596	157.0	117.7	144.1	#1^{P}	9.3	9.3	20	115	6.3 ± 2.9	84 ± 42	✓
					#2^{P}	10.0	10.0	20	356	7.8 ± 3.6	107 ± 54	…
SPT-CLJ0156–5541	1.2	<0.02	1.2	<0.02	#1^{P}	20.9	20.9	40	139	2.5 ± 1.1	3.8 ± 1.9	✓[a]
					#2^{P}	21.2	39.0	40	335	4.6 ± 2.1	9.8 ± 4.9	…
SPT-CLJ2342–5411	1.075	3.1	1.8	0.7	#1^{P}	13.9	13.9	26	196	0.9 ± 0.4	2.8 ± 1.4	×

Note. The first division contains the six systems with visually convincing cavities, while the second contains the two systems with marginally visually convincing cavities; see paragraph 4 in Section 3.2 for details. (1) Name; (2) redshift; (3) bolometric cooling luminosity within which $t_{\rm cool}$ is equal to 7.7 Gyr; (4) same but defined within $r = 50$ kpc; (5) same but defined within which $t_{\rm cool}$ is equal to the look-back time since $z = 2$; (6) cavity number (N) with the depth of the cavity compared to the surrounding X-ray emission: C for "clear" and P for "Potential"; see Section 3.1; (7) cavity radius along the jet (errors are ±20%); (8) cavity radius perpendicular to the jet (errors are ±20%); (9) distance from the central AGN to the center of the cavity; (10) position angle of the cavity for north to east; (11) cavity enthalpy; (12) cavity power; (13) radio emission associated with AGNs in the BCG.

[a] Radio source not centered on the BCG.

[b] Dynamic range limited by the presence of a nearby, un-associated, bright radio source.

[c] Phoenix cluster (e.g., McDonald et al. 2012).

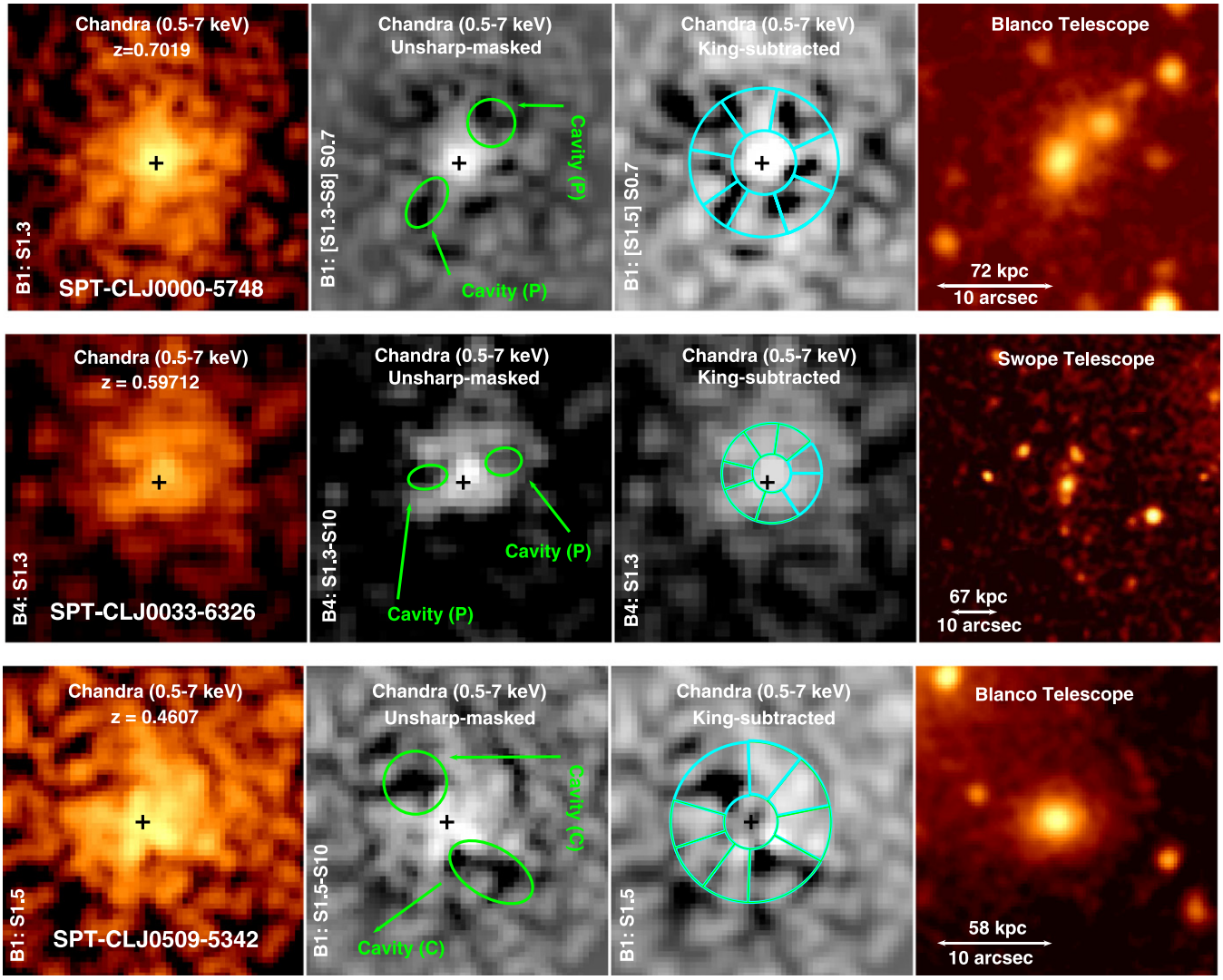

Figure 2. Images of the SPT–SZ clusters with candidate X-ray cavities. For each row, we show the candidate cluster's 0.5–7 keV X-ray image, the 0.5–7 keV unsharp-masked image, the 0.5–7 keV King-subtracted image, and the optical or infrared image. The position of the central AGN, taken to be the position of the BCG, is shown with the black cross. The smoothing and binning factors are shown in the lower-left corners. We also highlight the cavities in green, as well as their depth: "C" ("P") for clear (potential), see Section 3.1. In light blue, we illustrate the annuli used to compute the azimuthal surface brightness profiles (Figure 3). Images of the SPT–SZ clusters with candidate X-ray cavities. See caption on page 4. Images of the SPT–SZ clusters with candidate X-ray cavities. See caption on page 4.

right panels of Figure 2). Each annulus was divided into eight azimuthal sectors, containing roughly 50 counts per sector. On average, the depressions lie $\sim 1\sigma$–3σ below the surrounding X-ray emission and contain 10%–40% less counts, roughly consistent with X-ray cavities seen in local clusters. Based on these results, we refer to the cavities lying 1σ–2σ below the surrounding X-ray emission as "potential" cavities (see "P" in Column 5 of Table 1), requiring deeper *Chandra* data to confirm them, while we refer to those lying 2σ–3σ (or more) below the surrounding X-ray emission as "clear" cavities (see "C" in Column 5 of Table 1). We note that the latter are only found among the six SPT–SZ clusters with visually "convincing" X-ray cavities, as explained earlier in this section.

In Table 1, we also highlight the SPT–SZ clusters with X-ray cavities that have a radio source associated with the central regions. Since all of the low-redshift clusters with X-ray cavities have a radio-active BCG, we expect this to be similarly the case for the SPT–SZ clusters with X-ray cavities. We use the 843 MHz Sydney University Molonglo Sky Survey (SUMSS, synthesized beam width of $\sim 40''$; Bock et al. 1999; Mauch et al. 2003), but owing to the large beam size, we cannot resolve any extended jet-like emission. We therefore use the radio data simply to verify that the clusters in our sample with X-ray cavities have radio-loud BCGs. We note that the radio sources in SPT-CLJ0033–6326 and SPT-CLJ0156–5541 are not centered on the BCG, but that the BCG lies well within the beam size of SUMSS. While the position uncertainty of sources detected in SUMSS is only $\sim 10''$, these BCGs may still contain a radio source that is contributing to the overall emission in the beam, since they lie well within the beam size. We therefore consider that these sources have a radio counterpart for the purposes of this paper. SPT-CLJ0509–5342 lies within two beam sizes of a nearby 120 mJy radio source, making its detection by SUMSS uncertain since SUMSS is dynamic range limited by 1:100 on average (Bock et al. 1999). This bright radio source is most likely not associated with the BCG since, at its redshift, it would be located some 700 kpc from the galaxy. Finally, we find no evidence from the SUMSS maps of a radio source in SPT-CLJ2342–5411. Considering that this source is the second most

distant cluster among our candidates ($z = 1.075$), the non-detection may simply be due to the limited sensitivity of the survey. In summary, and as expected, the majority of clusters with clear X-ray cavities (Table 1) have a detected radio counterpart.

3.2. Cavity Energetics

To study the evolution of AGN feedback in BCGs, the energetics of the X-ray cavities in the SPT–SZ sample must be computed. These are estimated using the standard techniques, which we describe below (see Bîrzan et al. 2004, and references therein). Assuming that the cavity is filled with a relativistic fluid, the total enthalpy is

$$E_{\rm bubble} = 4pV, \quad (2)$$

where p is the thermal pressure of the ICM at the radius of the bubble (estimated from X-ray data, assuming $p = n_e kT$) and V is the volume of the cavity. We assume that the cavities are of prolate shape. The volume is then given by $V = 4\pi R_{\rm w}^2 R_{\rm l}/3$, where $R_{\rm l}$ is the projected semimajor axis along the direction of the jet and $R_{\rm w}$ is the projected semimajor axis perpendicular to the direction of the jet. Errors on the radii are assumed to be ±20%, and the jet is defined as the line that connects the central AGN to the middle of the cavity. The position of the central AGN is chosen to coincide with the position of the BCG as seen from the optical or infrared images (Figure 2). If two central dominant galaxies were present in the optical images, we chose the brightest one as the BCG. There is only one cluster where this applies: SPT-CLJ0616–5227. Modifying the location of the BCG to coincide with the second dominant galaxies modifies the cavity energetics by a factor of $\leqslant 2$, which is not significant for the purposes of this study.

In Table 1, we give the constraints on the X-ray cavity radii ($R_{\rm l}$ and $R_{\rm w}$), enthalpy (pV), and cavity power ($P_{\rm cav}$). Cavity powers are determined by dividing the total enthalpy of the X-ray cavity ($4pV$) by its age. The latter is given by the buoyancy rise time (Churazov et al. 2001):

$$t_{\rm buoyancy} = R\sqrt{\frac{SC_{\rm D}}{2gV}}. \quad (3)$$

Here, R is the projected distance from the central AGN to the middle of the cavity, S is the cross-sectional area of the bubble ($S = \pi R_{\rm w}^2$), $C_{\rm D}$ is the drag coefficient (assumed to be 0.75;

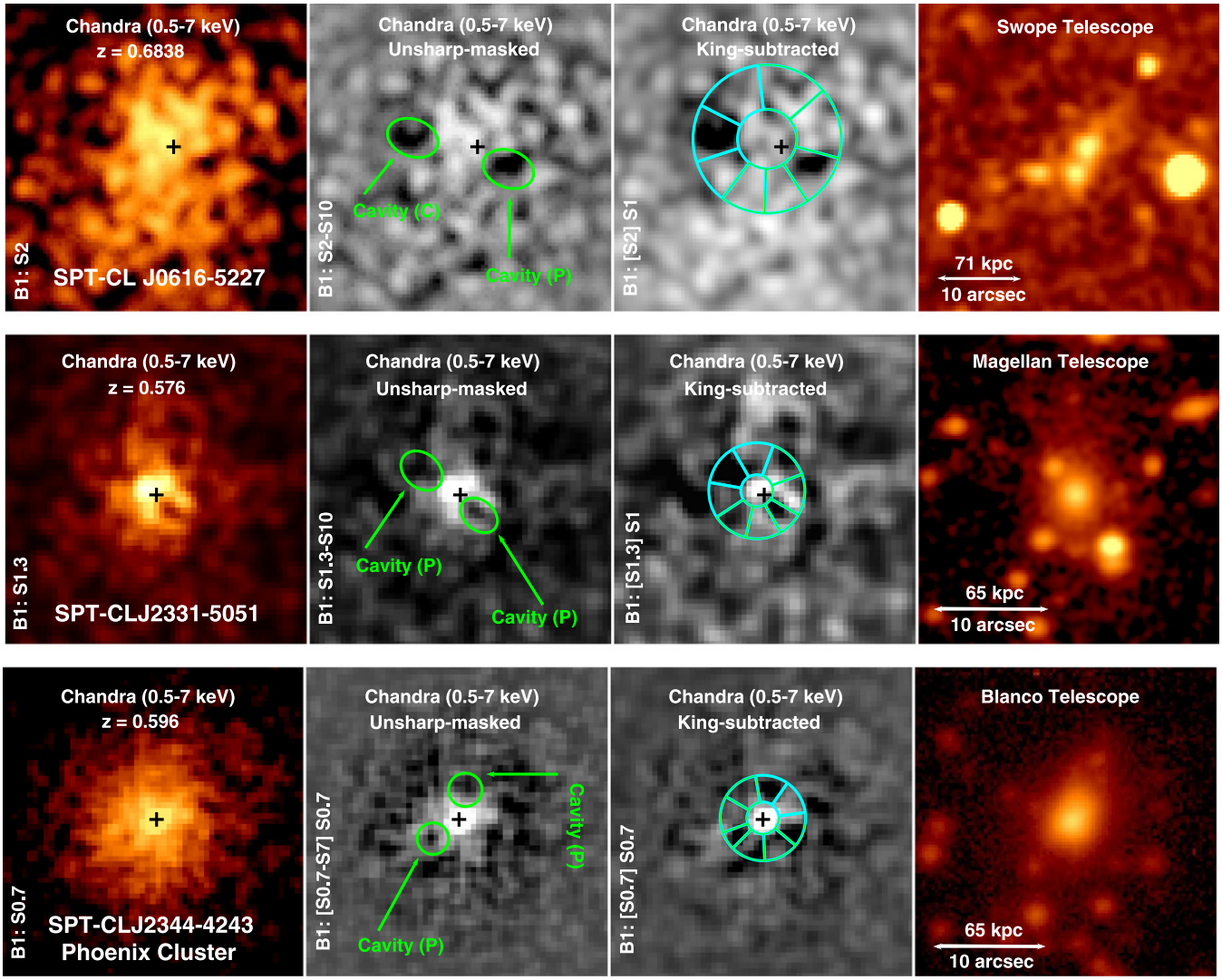

Figure 2. (Continued.)

Churazov et al. 2001), and g is the local gravitational potential. We use the values of g derived by M13 (see resulting values in Table 1) but stress that the typical uncertainties are larger than those reported in M13: they are on the order of $\pm 50\%$, as mentioned in Section 2. The enthalpy and powers of the X-ray cavities in the SPT–SZ sample are therefore known, at best, to within a factor of a few.

4. COOLING LUMINOSITIES

Ultimately, we wish to determine if AGN feedback is operating differently in high-redshift clusters and, in particular, if AGN feedback is able to suppress cooling of the hot ICM at early times. We can address this question by comparing the mechanical energy injection (measured from X-ray cavities) to the energy lost by cooling. The latter is often quoted in terms of the cooling luminosity ($L_{\rm cool}$), defined as the bolometric X-ray luminosity ($0.01-100$ keV) interior to the radius where the cooling time is equal to some threshold value. We adopt several definitions of this value throughout this paper.

The first definition is motivated by earlier studies on X-ray cavities, including those by Nulsen et al. (2009), Rafferty et al. (2006), and HL12. These studies defined the cooling luminosity to be the bolometric X-ray luminosity within which the cooling time is equal to 7.7 Gyr (Column 3 in Table 1). For the clusters in this sample, this definition effectively measures the total cooling occurring within a radius of $\lesssim$100 kpc (see Table 1). As in HL12, we define the cooling time to be

$$t_{\rm cool} = \frac{5}{2}\frac{n\,kT\,V}{L_{\rm X}}. \quad (4)$$

Here, n is the total number of gas particles per unit volume, kT is the gas temperature, $L_{\rm X}$ is the gas bolometric X-ray luminosity, and V is the gas volume contained within each annulus. In addition to the internal energy of the gas ($3/2 \times nkT$), the enthalpy includes the work done on the gas as it cools at constant pressure in Equation (4) ($5/2 \times nkT$). Nulsen et al. (2009) calculate their cooling luminosities within a radius where the cooling time is 7.7 Gyr, but they do not specify whether these luminosities are bolometric luminosities. Since their sample contains only lower-mass systems, we only compare our study to theirs qualitatively. Rafferty et al. (2006) calculate their bolometric cooling luminosities at 7.7 Gyr, but they do not specify the equation they use for the cooling time. In HL13, we recalculated the cooling luminosities using Equation (4) for all the massive clusters in Rafferty et al. (2006; 14 in total). We found our values to be consistent with theirs within 1σ of the scatter in the population, although ours were systematically smaller. Overall, there is no significant difference, at least for the purposes of this study, and we proceed to directly compare our results with Rafferty et al. (2006).

The second definition, chosen to be the bolometric X-ray luminosity within $r = 50$ kpc (Column 4 of Table 1), is more physically motivated. This definition allows us to directly compare the heating and cooling within (roughly) the same volume. The values we obtain with this second definition are 20%–40% smaller compared to those obtained at 7.7 Gyr.

Finally, we adopt a third definition, motivated by the results of M13 (Column 5 of Table 1). M13 estimated that cool cores

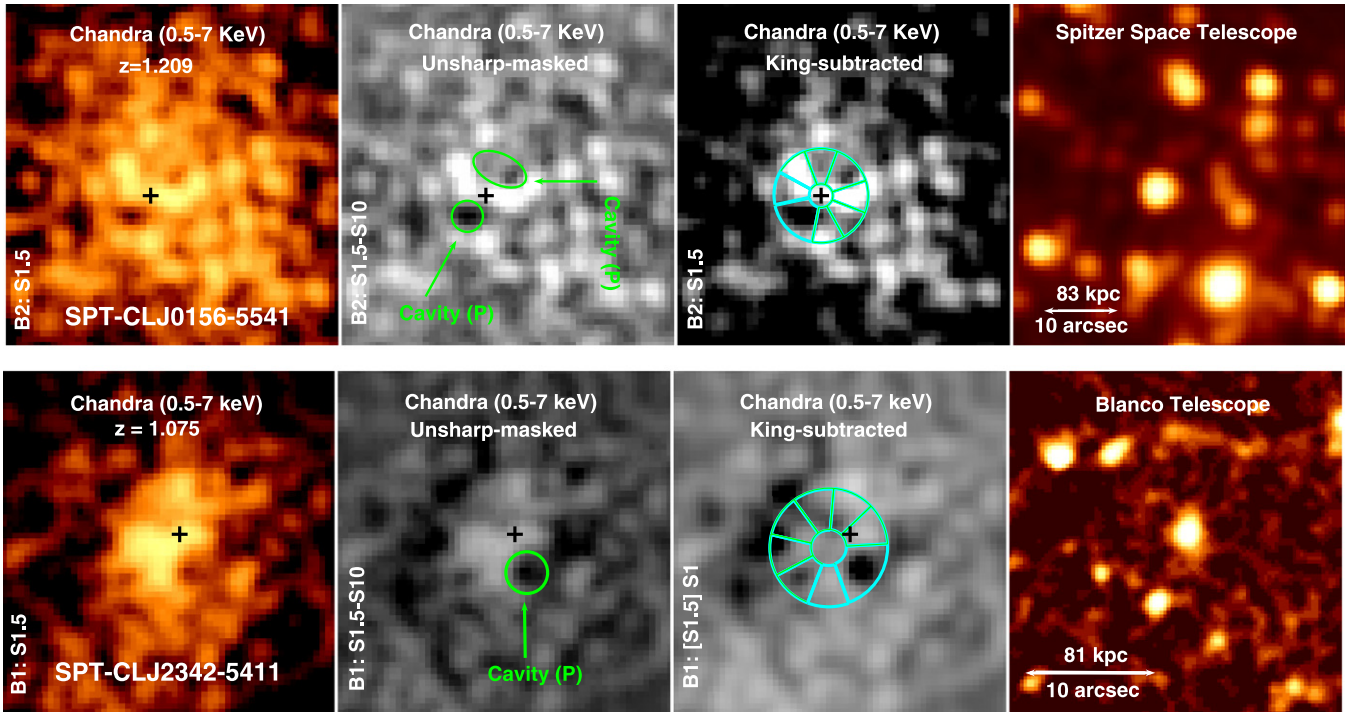

Figure 2. (Continued.)

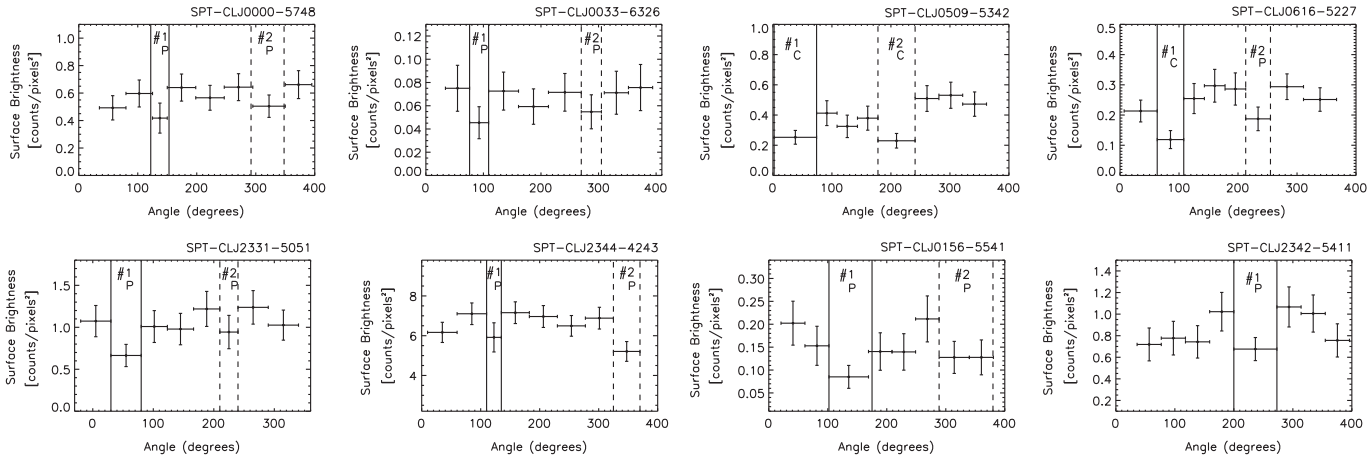

Figure 3. We show the 0.5−7 keV azimuthal surface brightness profile of the annuli containing the candidate cavities (Figure 2). The vertical lines illustrate the locations of each cavity. These plots show that the majority of the X-ray cavities lie $\sim 1\sigma - 3\sigma$ below the surrounding X-ray emission. We also indicate the depth of the X-ray cavities: "C" ("P") for clear (potential); see Section 3.1.

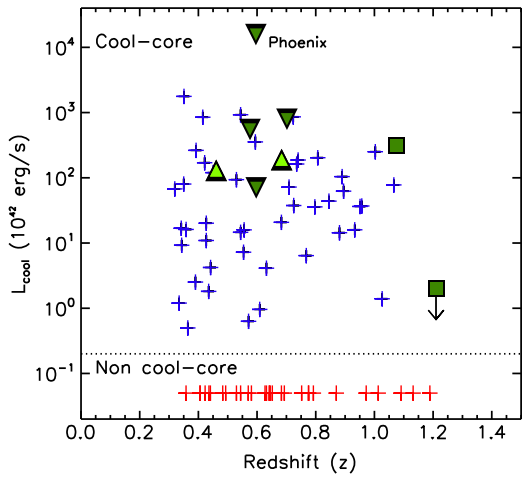

Figure 4. Cooling luminosities ($L_{\rm cool}$) at 7.7 Gyr as a function of redshift for the 83 SPT–SZ clusters with *Chandra* X-ray observations. The cool cores, where the cooling time drops below 7.7 Gyr, are shown in blue and the non-cool cores in red. For the latter, we assign an arbitrary low $L_{\rm cool}$ value below the dotted line for illustrative purposes. Highlighted in green are the systems in which we identified candidate X-ray cavities. The different shades of green highlight the depth of the cavities compared to the surrounding X-ray emission with light (dark) green for the "clear" ("potential") cavities. The clusters with convincing cavities are shown with the triangles, while SPT-CLJ0156–5541 and SPT-CLJ2342–5411are shown with the squares, as discussed in Section 3.1.

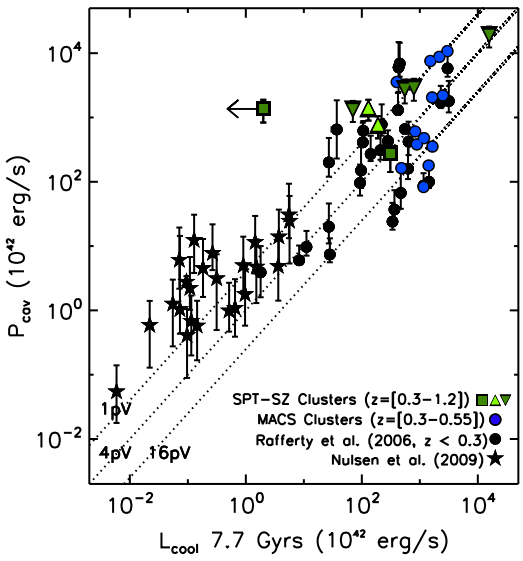

Figure 5. Comparison between the mechanical power being injected by the AGN in the BCG ($P_{\rm cav}$) and the cooling luminosity ($L_{\rm cool}$) of the cluster at 7.7 Gyrs. The SPT–SZ clusters with candidate X-ray cavities are shown in green. We use triangles to highlight the six SPT–SZ clusters with convincing X-ray cavities, while squares are used for SPT-CLJ0156–5541 and SPT-CLJ2342–5411 as discussed in Section 3.1. Furthermore, the different shades of green highlight the depth of the cavity compared to the surrounding X-ray emission with light (dark) green for the "clear" ("potential") cavities. We note that the $P_{\rm cav}$ values are uncertain by a factor of a few for the SPT–SZ clusters as discussed in Section 2.

began to assemble in massive systems at $z = 1^{+1.0}_{-0.2}$, implying that only a small fraction of the ICM in high-redshift clusters would have had the time to cool completely, form cold molecular gas, and feed the black hole that is generating the X-ray cavities. As such, we define a third cooling luminosity to be the bolometric X-ray luminosity within which the cooling time is equal to the look-back time since $z = 2$. The new values with this third definition are 10%–95% smaller compared to those obtained at 7.7 Gyrs. For the 13 MACS clusters with X-ray cavities (HL12), we also computed cooling luminosities using this third definition and find that the new values are only ∼10% smaller. It therefore remains appropriate to use the definition of the cooling luminosity at 7.7 Gyrs for MACS clusters ($z_{\rm average} \sim 0.4$). The difference only becomes significant for higher-redshift clusters, such as those presented in this work ($z_{\rm average} \sim 0.7$).

5. RESULTS

5.1. Distribution of X-ray Cavities

In Figure 4, we plot the cooling luminosity of the 83 SPT–SZ clusters with *Chandra* observations using the standard 7.7 Gyrs cooling time definition. This plot shows that the majority of the SPT–SZ clusters with X-ray cavities lie in the strongest cool-core clusters. This is expected in part since the majority of the counts in the *Chandra* X-ray images will be concentrated toward the central regions for cool-core clusters, due to highly peaked X-ray surface brightness distributions. This higher concentration of counts in the central regions makes it easier to identify depressions.

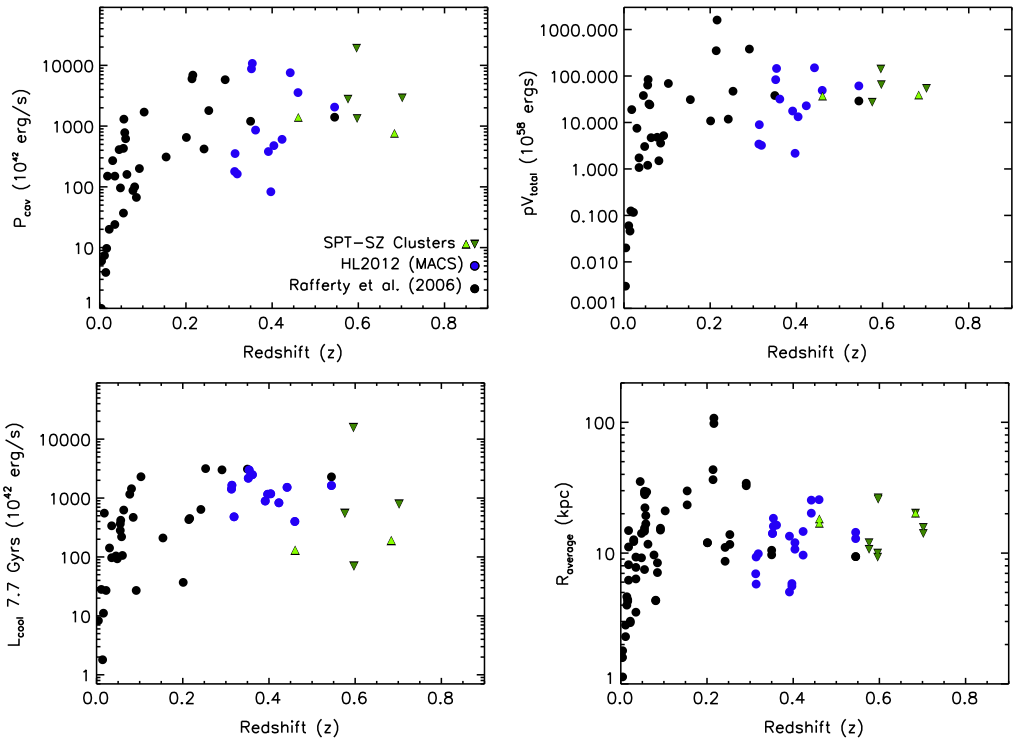

Figure 6. Plots of the mechanical power of X-ray cavities ($P_{\rm cav}$, top left), the enthalpy of the X-ray cavities ($PV_{\rm total}$, top right), and the cooling luminosity as defined with the 7.7 Gyrs threshold ($L_{\rm cool}$, bottom left) for each cluster, as a function of redshift. Note that the $P_{\rm cav}$ and $PV_{\rm total}$ values are usually uncertain by at least a factor of a few, especially for SPT–SZ clusters as discussed in Section 2. We also show the average radius of *each* cavity ($R_{\rm average}$, bottom right) as a function of redshift. Same symbols as Figure 5. Here, we focus only on the SPT–SZ clusters with visually convincing cavities and therefore exclude SPT-CLJ0156–5541 and SPT-CLJ2342–5411 from these plots.

5.2. Energetics of X-ray Cavities

AGN feedback in clusters of galaxies is known to be finely tuned to the energy needed to offset cooling of the hot ICM out to $z \sim 0.6$ (HL12). We illustrate this in Figure 5, where we plot data points from Nulsen et al. (2009, black circles), Nulsen et al. (2009, black stars) and HL12 (blue circles). In green, we show the SPT–SZ clusters with X-ray cavities. Here, we adopt the first definition of the cooling luminosity, defined as the bolometric X-ray luminosity within which the cooling time is equal to 7.7 Gyrs. Figure 5 shows that, on average, X-ray cavities can offset cooling of the hot ICM even in the highest-redshift sources. We note that this result remains true if we use the other two definitions of the cooling luminosity (see Section 4). We discuss these results in Section 6.4.1.

5.3. Redshift Distribution of X-ray Cavities

In Figure 6, we address whether AGN feedback in clusters of galaxies, as probed by the presence and properties of X-ray cavities, is evolving significantly with redshift. In this figure, we plot the mechanical power of the X-ray cavities ($P_{\rm cav}$), the enthalpy of the X-ray cavities ($PV_{\rm total}$), and the cooling luminosity defined with the 7.7 Gyrs threshold ($L_{\rm cool}$) for each cluster, as a function of redshift. In the bottom right panel, we also plot the average X-ray cavity radius $R_{\rm average}$ defined as $(R_l \times R_{\rm w})^{1/2}$ for *each* X-ray cavity. Since we plot the radius for *each* cavity, there are more data points in this panel. We only include the objects in Rafferty et al. (2006, black circles) and HL12 (blue circles) since Nulsen et al. (2009) do not provide any redshift information. In these plots and for the remainder of the paper, we focus only on the systems with convincing cavities (i.e., we exclude SPT-CLJ0156–5541 and SPT-CLJ2342–5411). Figure 6 shows that there is no significant evolution in any of the cavity properties for the largest and most powerful outflows. To provide a first-order correction for the dependency of mass on the cavity powers, we also plot in Figure 6 the ratio between the mechanical power and the cooling luminosity as a function of redshift. As we will discuss in Section 6.1, we are strongly biased against finding small cavities ($r \lesssim 10$ kpc) in the XVP *Chandra* data. Removing these small cavities from Figure 7 for the lower-redshift samples does not affect the results. We further discuss Figures 5 and 6 in Section 6.4.1.

6. DISCUSSION

We have visually inspected the *Chandra* X-ray images of a sample of 83 SPT–SZ clusters located at $0.3 < z < 1.2$ and found that six clusters contain visually convincing surface brightness depressions that we interpret to be X-ray cavities. By comparing the X-ray emission within the cavities to the surrounding X-ray emission, we determined the depth of the cavities in each system and classified them into two distinct categories: those with "potential" cavities (4/6 clusters) when the cavity emission was only $1\sigma-2\sigma$ below the surrounding X-ray emission and those with "clear" cavities (2/6) when the cavity emission was at least $2\sigma-3\sigma$ below the surrounding X-ray emission. While deeper *Chandra* observations are needed to confirm the "potential" cavities, we proceed with the discussion of these results. We first discuss the various selection effects that may be present in this study, and then we discuss the implications of this study.

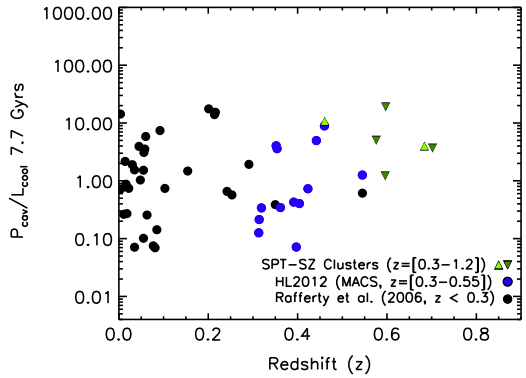

Figure 7. Plot showing the ratio between the mechanical power of X-ray cavities (P_{cav}) and the cooling luminosity (L_{cool}) at 7.7. Gyrs for different samples of clusters, as a function of redshift. We also exclude SPT-CLJ0156–5541 and SPT-CLJ2342–5411 from these plots, as in Figure 5.

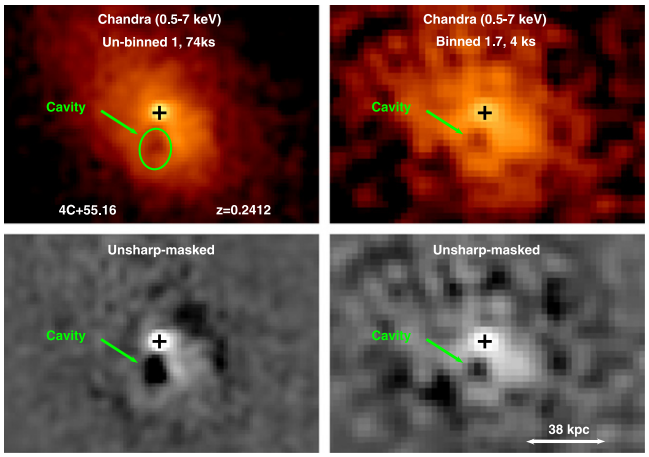

Figure 8. *Chandra* X-ray images of 4C+55.16 ($z = 0.2412$). Left: un-binned image (74 ks, ~40,000 counts, top) and corresponding unsharp-masked image (bottom). Right: limited exposure image (4 ks, ~2000 counts, top) binned by a factor of 1.7 to mimic its appearance as if it were at the average redshift of the SPT–SZ clusters with X-ray cavities ($z \sim 0.7$), and corresponding unsharp-masked image (bottom). This figure shows that the southern X-ray cavity remains visible in all X-ray images.

6.1. Selection Effects

While the results presented in Section 5 are interesting, there may be several biases present in the cavity selection method and the analysis. Below we address these potential biases.

First, we will clearly miss cavities below the resolution limit ($R_{\rm average} \lesssim$ 10 kpc; see Table 1), as well as those that lie on a jet axis parallel to our line of sight. Furthermore, we limited the search to the central regions of each cluster, where most of the X-ray counts are located, and disregarded any X-ray depression identified at $r > 100$ kpc. Future, deeper X-ray observations would be necessary to detect these more extended cavities. We are likely therefore to miss any extremely large cavities like those in MS 0735.6+7421. Although these are expected to be energetically very important, they are expected to be rare with only two such systems currently known (McNamara & Nulsen 2007).

In Figure 8, we show the *Chandra* X-ray images of the massive galaxy cluster 4C+55.16 ($z = 0.2412$, Iwasawa et al. 2001; Hlavacek-Larrondo et al. 2011). The left panels show the deep *Chandra* images (74 ks), which reveal a large southern X-ray cavity. The right panels show the same image but for a

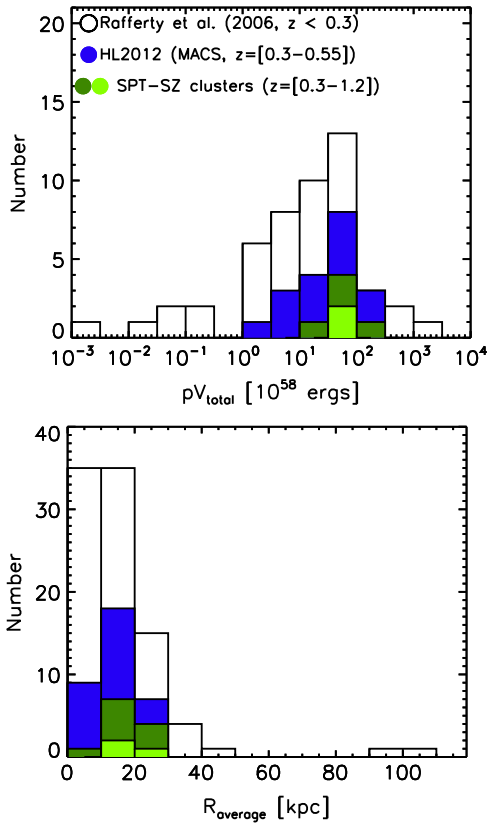

Figure 9. Plots highlighting the distribution of cavity enthalpy (top) and the average cavity radius (bottom). As in Figures 5 and 6, we exclude SPT-CLJ0156–5541 and SPT-CLJ2342–5411 from these plots.

reduced exposure time of only 4 ks and binned by a factor of 1.7 (pixel size of 0.″836 × 0.″836) to mimic the appearance of the cluster as if it were located at the average redshift of the SPT–SZ clusters with X-ray cavities ($z \sim 0.7$). We reduce the exposure time to 4 ks since this reduces the total number of cluster counts to ~2000, similar to the counts in the *Chandra* X-ray images of the SPT–SZ clusters. Figure 8 shows that the cavity in 4C+55.16 remains visible in all panels. According to our criteria described in Section 3.1, we would identify this X-ray cavity as a "potential" cavity since the cavity emission lies only 1σ–2σ below the surrounding X-ray emission. We note that adding an additional 75 ks blank field exposure to the images, mimicking the increase in background from the long exposure needed to get 2000 counts for high-redshift clusters, does not change our results.

Even though Figure 8 demonstrates that we can identify cavities with as few as 2000 counts, we are likely missing several cavities due to limited data quality of the 83 SPT–SZ clusters with *Chandra* observations. To test the probability of identifying cavities in the SPT–SZ cluster survey, we applied the same imaging processes as in Figure 8 to the 13 MACS clusters with X-ray cavities: we reduced the exposure times such that each cluster contained only ~2000 counts and binned the images to mimic the appearance of each cluster as if it were located at $z \sim 0.7$. Interestingly, we found that only ~60% of these X-ray cavities would then have been detected using the same criteria as those in Section 3.1, and that an even smaller fraction (~20%) would have had "clear" cavities with a cavity emission 2σ–3σ (or more) below the surrounding X-ray emission, as defined in Section 3.1. This demonstrates that

we are likely missing cavities in the SPT–SZ sample due to the limited X-ray depth of the survey (see also Enßlin & Heinz 2002; Diehl et al. 2008; Bîrzan et al. 2012). Moreover, the strongly peaked X-ray surface brightness distributions of strong cool-core clusters also imply that the X-ray counts will be highly concentrated toward the central regions in these clusters. We may therefore be preferentially selecting X-ray cavities in strong cool-core clusters.

Simulations have shown that the increased SZ signal due to the presence of a cool core is not significant (Motl et al. 2005; Pipino & Pierpaoli 2010), and that, similarly, star formation does not fill in the SZ decrement significantly (e.g., McDonald et al. 2012). In particular, Lin et al. (2009) showed that at $z = 0.6$, less than 2% of clusters with a mass exceeding $10^{14}\ M_{\odot}$ will host a radio AGN that contributes to more than 20% of the SZ signal, even when accounting for the fraction of systems with flat or inverted spectra. This fraction is even smaller at higher redshift due to the decreasing flux. These biases should therefore not be significant.

Finally, we recall that the majority of the cavities presented here lie only $1\sigma-2\sigma$ below the surrounding X-ray emission. These depressions could therefore be caused by other activity in the cluster such as merger-induced asymmetries in the X-ray gas distribution. This is especially true for SPT–SZ clusters, since cluster merger rates are expected to increase with redshift (e.g., Cohn & White 2005; Ettori & Brighenti 2008). It is also important to note that cluster mergers can provide an additional source of heating to the X-ray gas. At high redshift, AGN feedback may therefore no longer be the only heating source of the ICM.

6.2. X-ray Cavity Detection

Out of the 83 SPT–SZ clusters with *Chandra* observations, we find that six clusters have visually convincing X-ray cavities. For these six systems, all of the cavities are found in pairs, most of which are similar in size and symmetrically located on either side of the AGN in the BCG. In Section 3.1, we also showed that these cavities lie $1\sigma-3\sigma$ below the surrounding X-ray emission. While the probability of having one $1\sigma-3\sigma$ random fluctuation in the *Chandra* X-ray images is high, due to the Poisson nature of the observations, the probability of having two such fluctuations in an eight-element azimuthal array, as in Figure 3, is substantially lower: ∼37% for two $\sim1\sigma$ fluctuations within $r = 100$ kpc. Moreover, the probability of having the two fluctuations at $180^{\circ} \pm 30^{\circ}$ from one another in PA is only ∼10%. If we also require them to have matching radii to within ±50 kpc in radius from one another, as observed in Table 1, then the number drops to ∼7.5% and even further for two $\sim2\sigma$ ($\lesssim$0.2%) and two $\sim3\sigma$ ($\lesssim$0.001%) fluctuations. Overall, the probability that the cavities presented here are caused by random fluctuations, given the PA and radii properties observed in Table 1, is very small. Instead, the depressions may well be cavities being carved out by twin radio lobes.

We note that all of these calculations were computed using a Monte Carlo approach, assuming a random normal distribution for the cavity flux and a random uniform distribution for the PAs and radii of the cavities. The statistics are also based on the annuli shown in Figure 3, which do not cover the full radial extent ($r < 100$ kpc) considered in the cavity selection. By adding additional spatial elements, we would increase the chance of a false detection (by adding more draws) but would also increase the significance of the individual detections (by improving the measurement of the "background"). Thus, we expect that these probabilities are within a factor of ∼2 of what one would get by doing a more rigorous analysis. In principle, it should also be possible to derive an approach, similar to the one used here, but focusing on the probability of finding $1\sigma-3\sigma$ fluctuations by eye within the entire region of $r < 100$ kpc. However, it is very difficult to quantify this selection function, as visual identification can vary significantly from one person to another. We therefore choose to focus only on reporting approximate probabilities in this paper, based on the annuli statistics shown in Figure 3.

6.3. X-ray Cavity Properties

In this section, we discuss various properties of the detected X-ray cavities in the SPT–SZ sample (e.g., Figure 9). First, we note that the average power, enthalpy, and radius of the cavities in the six SPT–SZ clusters with convincing X-ray cavities are $\sim5 \times 10^{45}$ erg s^{-1}, $\sim6 \times 10^{59}$ erg, and ∼16 kpc, respectively, whereas the average cooling luminosity for these same clusters is $\sim(2-3) \times 10^{45}$ erg s^{-1} (depending on which definition we adopt; see Section 4). The X-ray cavities in these six SPT–SZ clusters therefore provide, on average, enough energy to offset cooling of the hot ICM. This statement remains true even if (1) we include SPT-CLJ0156–5541 and SPT-CLJ2342–5411 in the calculations and (2) we only consider the two SPT–SZ clusters with "clear" cavities (SPT-CLJ0509–5342 and SPT-CLJ0616–5227) where the cavity emission lies $2\sigma-3\sigma$ below the surrounding emission. For the latter, the average cavity power, enthalpy, and radius would be $\sim0.8 \times 10^{45}$ erg s^{-1}, $\sim3 \times 10^{59}$ erg, and ∼18 kpc, respectively, whereas the average cooling luminosity would be $\sim0.1 \times 10^{45}$ erg s^{-1}.

We also note that the detection fraction in the sample is 7% since 6 of the 83 SPT–SZ clusters with *Chandra* observations have visually convincing X-ray cavities. If we only consider the two clusters with "clear" cavities, then the fraction drops to 2%. This is a factor of several less than the fraction observed in local clusters, where the fraction with X-ray cavities is 20%–30% (Dunn & Fabian 2006; Rafferty et al. 2006; Bîrzan et al. 2012; Fabian 2012; HL12). However, our result is more likely a lower limit, due to selection effects (see Section 6.1), which will need to be quantified with deeper observations and studies of other cluster samples at high redshifts.

6.4. Evolution of X-ray Cavity Properties

6.4.1. Implications for AGN Feedback

Interestingly, M13 analyzed the cooling properties of the same 83 SPT–SZ clusters with *Chandra* observations as those studied here and found that stable long-standing feedback is required to halt cooling of the hot ICM to low temperatures. In agreement with M13, Figures 5 and 7 show that the enthalpy of X-ray cavities ($pV_{\rm tot}$) does not vary significantly with redshift out to $z \sim 0.8$. These results imply that powerful mechanical feedback may have been operating in massive clusters of galaxies for over half of the age of the universe (>7 Gyrs, corresponding to the look-back time since $z \sim 0.8$). Newly discovered high-redshift clusters such as WARPJ1415.1+3612 (Santos et al. 2012) also find that radio-mode feedback must have already been established at $z \sim 1$.

In Section 6.3, we found that the average cavity power of the six SPT–SZ clusters with convincing cavities was higher than their average cooling luminosity. In fact, they appear to be injecting an excess of $\sim 2 \times 10^{45}$ erg s^{-1} in heat. According to Figure 7, this excess is most significant for the clusters in the SPT–SZ sample, in particular, at $z \gtrsim 0.5$. Assuming that AGN duty cycles remain high and that heating is roughly constant out to $z \sim 1$, as suggested by Santos et al. (2012), the excess heat amounts to ~1.0 keV per particle for a total gas mass of $5 \times 10^{13}\, M_{\odot}$. Although this result is based only on six objects, the excess heat is similar to the energy needed to explain the excess entropy in clusters (Kaiser 1991; Voit 2005) and would be ~30% larger assuming that the excess heat was being injected out to the onset of cool cores at $z \sim 2$ (M13). X-ray cavity powers are also likely only lower limits to the total energy injected by the central AGN, as weak shocks (McNamara et al. 2005; Fabian et al. 2006; Forman et al. 2007) and sound waves (Fabian et al. 2003; Sanders & Fabian 2008; Blanton et al. 2011) contribute to the total energy (see also Nusser et al. 2006; Mathews & Brighenti 2008). If confirmed, the excess heat could therefore be even larger.

Although intriguing, we stress that these calculations assume that all of the cavities in the six SPT–SZ clusters are real. If we only consider the two SPT–SZ clusters with "clear" cavities (SPT-CLJ0509–5342 and SPT-CLJ0616–5227), the excess heat would be ~0.7 $\times 10^{45}$ erg s^{-1} (or 0.4 keV per particle). The estimated excess heat injected per particle also depends on the duty cycle of the energy injection. For local BCGs, this duty cycle has been observed to be high (e.g., >60%–90%; Bîrzan et al. 2012; Fabian 2012). However, the lower limit in the SPT–SZ sample is ~11%, since 6 of the 52 clusters with signs of cooling have cavities (Figure 4). Applying this lower limit, we find that the excess in heat is reduced to 0.05–0.1 keV per particle for cool core clusters. We note that if duty cycles are decreasing with increasing redshift, AGN feedback may no longer be able to suppress all of the ICM cooling. In this case, we would expect to see an average increase in star formation rates for BCGs with increasing redshift. This may explain the unusually high star formation rate in the Phoenix cluster (McDonald et al. 2012, 2013b).

In summary, our results suggest that the AGNs in BCGs may be depositing as little as 0.1 keV per particle or as much as 1.0 keV per particle in excess heat, depending on whether the AGN duty cycles evolve or not between $z = 0$ and $z \sim 1$.

6.4.2. Implications for Supermassive Black Hole Growth

Our results show that powerful radio mode feedback may be operating in massive clusters of galaxies for over half of the age of the universe (>7 Gyrs, corresponding to the look-back time since $z \sim 0.8$). If we assume once more that the duty cycles of the AGNs in BCGs remain high, as they do for local BCGs, then this implies that the supermassive black holes in BCGs may have accreted a substantial amount of mass to power the X-ray cavities. To determine this, we use the following equation relating the jet (or cavity) power ($P_{\rm cav}$) to the black hole accretion rate ($\dot{M}$):

$$P_{\rm cav} = \eta \dot{M} c^2, \quad (5)$$

where η is the efficiency and c is the speed of light. We assume that the conversion efficiency between accreted mass and jet power is $\eta = 0.1$ (Churazov et al. 2005; Merloni & Heinz 2008; Gaspari et al. 2012) but stress that if it were lower, then the black holes would need to accrete even more mass. Assuming that the average jet power of SPT–SZ clusters with X-ray cavities is a representative value for massive cool core clusters ($(0.8-5) \times 10^{45}$ erg s^{-1}), and integrating Equation (5) over 7 Gyrs while assuming nearly constant duty cycles, we find that the supermassive black holes in these BCGs must have accreted $(1-6) \times 10^9\, M_{\odot}$ in mass to power the radio jets responsible for carving out the observed X-ray cavities. If correct, this would imply that supermassive black hole growth in BCGs may be important not only at earlier times during quasar mode feedback, when the black holes are accreting at rates near the Eddington limit (see Alexander & Hickox 2012, for a review), but also at later times when the black holes are accreting at low rates and driving powerful jetted outflows (see also HL12; Ma et al. 2013). We note that if we only consider the lower limit to the duty cycle (11% for cool core clusters), then the accreted mass is $(0.1-1) \times 10^9\, M_{\odot}$ and remains substantial.

7. CONCLUDING REMARKS

We have performed a visual inspection of *Chandra* X-ray images for 83 SPT–SZ galaxy clusters, finding that six contain visually convincing X-ray cavities. These cavities are likely the result of mechanical, or "radio-mode," feedback from the central supermassive black hole. This works extends the previous samples of known X-ray cavities to higher redshift (from $z \sim 0.5$ to $z \sim 0.8$). Interestingly, we find that the Phoenix cluster ($z = 0.596$) is one of these six systems with X-ray cavities (see also M. McDonald et al. 2015, in preparation), and that its extreme cavity power of $P_{\rm cav} \sim 2 \times 10^{46}$ erg s^{-1} rivals those in MS 0735.6+7421 (McNamara et al. 2005). On average, the SPT–SZ clusters with detected X-ray cavities have cavity powers of $(0.8-5) \times 10^{45}$ erg s^{-1}, enthalpies of $(3-6) \times 10^{59}$ erg, and radii of ~17 kpc. We identify two additional systems at $z \sim 1$ that contain marginally detected cavities. Overall, this work suggests that powerful mechanical feedback may have been operating in massive clusters of galaxies for over half of the age of the universe (>7 Gyrs). We stress, however, the importance of deep *Chandra* follow-up to confirm and further analyze these structures, and that these results are only based on a few objects.

J.H.L. is supported by NASA through the Einstein Fellowship Program, grant number PF2-130094, NSERC through the discovery grant and Canada Research Chair programs, as well as FRQNT. Partial support is also provided by the National Science Foundation through grants ANT-0638937 and PLR-1248097, the NSF Physics Frontier Center grant PHY-0114422 to the Kavli Institute of Cosmological Physics at the University of Chicago, the Kavli Foundation, and the Gordon and Betty Moore Foundation. Support for X-ray analysis was provided by NASA through *Chandra* Award Numbers 12800071, 12800088, and 13800883 issued by the *Chandra* X-ray Observatory Center, which is operated by the Smithsonian Astrophysical Observatory for and on behalf of NASA. Galaxy cluster research at Harvard is supported by NSF grant AST-1009012 and at SAO in part by NSF grants AST-1009649 and MRI-0723073. This work was supported in part by the U.S.

Department of Energy contract numbers DE-AC02-06CH11357 and DE-AC02-76SF00515.

Facilities: Blanco, *Magellan*: Baade, *Magellan*: Clay, *Spitzer*, South Pole Telescope, Swope, Chandra, Molonglo Observatory Synthesis Telescope (MOST).

REFERENCES

Alexander, D. M., & Hickox, R. C. 2012, NewAR, 56, 93
Benson, B. A., de Haan, T., Dudley, J. P., et al. 2013, ApJ, 763, 147
Bîrzan, L., McNamara, B. R., Nulsen, P. E. J., Carilli, C. L., & Wise, M. W. 2008, ApJ, 686, 859
Bîrzan, L., Rafferty, D. A., McNamara, B. R., Wise, M. W., & Nulsen, P. E. J. 2004, ApJ, 607, 800
Bîrzan, L., Rafferty, D. A., Nulsen, P. E. J., et al. 2012, MNRAS, 427, 3468
Blanton, E. L., Randall, S. W., Clarke, T. E., et al. 2011, ApJ, 737, 99
Blanton, E. L., Randall, S. W., Douglass, E. M., et al. 2009, ApJL, 697, L95
Bleem, L. E., Stalder, B., de Haan, T., et al. 2015, ApJS, 216, 27
Bock, D. C.-J., Large, M. I., & Sadler, E. M. 1999, AJ, 117, 1578
Burenin, R. A., Vikhlinin, A., Hornstrup, A., et al. 2007, ApJS, 172, 561
Cavagnolo, K. W., McNamara, B. R., Nulsen, P. E. J., et al. 2010, ApJ, 720, 1066
Churazov, E., Brüggen, M., Kaiser, C. R., Böhringer, H., & Forman, W. 2001, ApJ, 554, 261
Churazov, E., Sazonov, S., Sunyaev, R., et al. 2005, MNRAS, 363, L91
Cohn, J. D., & White, M. 2005, APh, 24, 316
Croton, D. J., Springe, V., White, S. D. M., et al. 2006, MNRAS, 365, 11
Diehl, S., Li, H., Fryer, C. L., & Rafferty, D. 2008, ApJ, 687, 173
Di Matteo, T., Springel, V., & Hernquist, L. 2005, Natur, 433, 604
Dong, R., Rasmussen, J., & Mulchaey, J. S. 2010, ApJ, 712, 883
Dunn, R. J. H., Allen, S. W., Taylor, G. B., et al. 2010, MNRAS, 404, 180
Dunn, R. J. H., & Fabian, A. C. 2006, MNRAS, 373, 959
Dunn, R. J. H., & Fabian, A. C. 2008, MNRAS, 385, 757
Dunn, R. J. H., Fabian, A. C., & Taylor, G. B. 2005, MNRAS, 364, 1343
Ebeling, H., Barrett, E., Donovan, D., et al. 2007, ApJL, 661, L33
Ebeling, H., Edge, A. C., & Henry, J. P. 2001, ApJ, 553, 668
Ebeling, H., Edge, A. C., Mantz, A., et al. 2010, MNRAS, 407, 83
Enßlin, T. A., & Heinz, S. 2002, A&A, 384, L27
Ettori, S., & Brighenti, F. 2008, MNRAS, 387, 631
Fabian, A. C. 2012, ARA&A, 50, 455
Fabian, A. C., Sanders, J. S., Allen, S. W., et al. 2003, MNRAS, 344, L43
Fabian, A. C., Sanders, J. S., Taylor, G. B., et al. 2006, MNRAS, 366, 417
Ferrarese, L., & Merritt, D. 2000, ApJL, 539, L9
Forman, W., Jones, C., Churazov, E., et al. 2007, ApJ, 665, 1057
Gaspari, M., Brighenti, F., & Temi, P. 2012, MNRAS, 424, 190
Gebhardt, K., Bender, R., Bower, G., et al. 2000, ApJL, 539, L13
Gioia, I. M., & Luppino, G. A. 1994, ApJS, 94, 583
Hasselfield, M., Hilton, M., Marriage, T. A., et al. 2013, JCAP, 7, 8
High, F. W., Stalder, B., Song, J., et al. 2010, ApJ, 723, 1736
Hlavacek-Larrondo, J., Fabian, A. C., Edge, A. C., et al. 2012, MNRAS, 421, 1360
Hlavacek-Larrondo, J., Fabian, A. C., Edge, A. C., et al. 2013, MNRAS, 431, 1638
Hlavacek-Larrondo, J., Fabian, A. C., Sanders, J. S., & Taylor, G. B. 2011, MNRAS, 415, 3520
Iwasawa, K., Fabian, A. C., Allen, S. W., & Ettori, S. 2001, MNRAS, 328, L5
Kaiser, N. 1991, ApJ, 383, 104
Körding, E. G., Jester, S., & Fender, R. 2006, MNRAS, 372, 1366
Kormendy, J., & Richstone, D. 1995, ARA&A, 33, 581
Lin, Y.-T., Partridge, B., Pober, J. C., et al. 2009, ApJ, 694, 992
Ma, C.-J., McNamara, B. R., & Nulsen, P. E. J. 2013, ApJ, 763, 63
Ma, C.-J., McNamara, B. R., Nulsen, P. E. J., Schaffer, R., & Vikhlinin, A. 2011, ApJ, 740, 51
Machacek, M. E., Jerius, D., Kraft, R., et al. 2011, ApJ, 743, 15
Magorrian, J., Tremaine, S., Richstone, D., et al. 1998, AJ, 115, 2285
Marriage, T. A., Acquaviva, V., Ade, P. A. R., et al. 2011, ApJ, 737, 61
Mathews, W. G., & Brighenti, F. 2008, ApJ, 685, 128
Mauch, T., Murphy, T., & Buttery, H. J. 2003, MNRAS, 342, 1117
McDonald, M., Bayliss, M., Benson, B. A., et al. 2012, Natur, 488, 349
McDonald, M., Benson, B., Veilleux, S., Bautz, M. W., & Reichardt, C. L. 2013b, ApJL, 765, L37
McDonald, M., Benson, B. A., Vikhlinin, A., et al. 2013a, ApJ, 774, 23
McNamara, B. R., & Nulsen, P. E. J. 2007, ARA&A, 45, 117
McNamara, B. R., & Nulsen, P. E. J. 2012, NJPh, 14, 055023
McNamara, B. R., Nulsen, P. E. J., Wise, M. W., et al. 2005, Natur, 433, 45
Merloni, A., & Heinz, S. 2008, MNRAS, 388, 1011
Motl, P. M., Hallman, E. J., Burns, J. O., & Norman, M. L. 2005, ApJL, 623, L63
Narayan, R., & Yi, I. 1994, ApJL, 428, L13
Nulsen, P., Jones, C., Forman, W., et al. 2009, in AIP Conf. Ser. 1201, Radio Mode Outbursts in Giant Elliptical Galaxies, ed. S. Heinz, & E. Wilcots (Melville, NY: AIP), 198
Nulsen, P. E. J., Jones, C., Forman, W. R., et al. 2007, in Heating versus Cooling in Galaxies and Clusters of Galaxies AGN Heating through Cavities and Shocks, ed. H. Böhringer et al. (Berlin: Springer), 210
Nusser, A., Silk, J., & Babul, A. 2006, MNRAS, 373, 739
O'Sullivan, E., Giacintucci, S., David, L. P., et al. 2011, ApJ, 735, 11
Pipino, A., & Pierpaoli, E. 2010, MNRAS, 404, 1603
Planck Collaboration, Ade, P. A. R., Aghanim, N., Armitage-Caplan, C., et al. 2013, arXiv:1303.5089
Planck Collaboration, Ade, P. A. R., Aghanim, N., Arnaud, M., et al. 2011, A&A, 536, A8
Rafferty, D. A., McNamara, B. R., Nulsen, P. E. J., & Wise, M. W. 2006, ApJ, 652, 216
Reichardt, C. L., Stalder, B., Bleem, L. E., et al. 2013, ApJ, 763, 127
Sanders, J. S., & Fabian, A. C. 2008, MNRAS, 390, L93
Sanders, J. S., Fabian, A. C., & Taylor, G. B. 2009, MNRAS, 393, 71
Santos, J. S., Tozzi, P., Rosati, P., Nonino, M., & Giovannini, G. 2012, A&A, 539, A105
Sifon, C., Menanteau, F., Hasselfield, M., et al. 2013, ApJ, 772, 25
Song, J., Zenteno, A., Stalder, B., et al. 2012, ApJ, 761, 22
Springel, V., White, S. D. M., Jenkins, A., et al. 2005, Natur, 435, 629
Staniszewski, Z., Ade, P. A. R., Aird, K. A., et al. 2009, ApJ, 701, 32
Sun, M., Voit, G. M., Donahue, M., et al. 2009, ApJ, 693, 1142
Ueda, S., Hayashida, K., Anabuki, N., et al. 2013, ApJ, 778, 33
Vanderlinde, K., Crawford, T. M., de Haan, T., et al. 2010, ApJ, 722, 1180
Vikhlinin, A., Kravtsov, A., Forman, W., et al. 2006, ApJ, 640, 691
Voit, G. M. 2005, RvMP, 77, 207
Wyithe, J. S. B., Turner, E. L., & Spergel, D. N. 2001, ApJ, 555, 504
Zhao, H. 1996, MNRAS, 278, 488